New insights on the defect sites evolution during CO oxidation over doped ceria nanocatalysts probed by in situ Raman spectroscopy

(Article begins on next page)

26 September 2024

New insights on the defect sites evolution during CO oxidation over doped ceria nanocatalysts probed by in situ Raman spectroscopy

Enrico Sartoretti[a,+], Chiara Novara[a,+], Marco Fontana[b], Fabrizio Giorgis[a], Marco Piumetti[a], Samir Bensaid[a]*, Nunzio Russo[a], Debora Fino[a]

[a] Department of Applied Science and Technology, Politecnico di Torino, Corso Duca degli Abruzzi, 24, 10129 Turin, Italy.

[b] Center for Sustainable Future Technologies, Istituto Italiano di Tecnologia, Via Livorno, 60, 10144 Turin, Italy.

* Corresponding author:

   E-mail address: samir.bensaid@polito.it (S. Bensaid).

[+] These authors contributed equally to this work.

ABSTRACT

Among the factors affecting ceria activity, the defectiveness plays a key role in the case of CO oxidation. In this study, its connection with the catalytic performance was investigated via in-situ Raman spectroscopy on nanostructured pure and Cu/Mn-doped ceria, monitoring the defect sites and surface species evolution during the reaction. The accumulation of polyene-like chains, formed through CO dissociative adsorption at the catalyst surface, was observed and their disappearance was related to the catalyst light-off temperature. Moreover, the doped samples exhibited a rise of the Raman bands associated to defects after the tests, consequence of the structural rearrangements occurring during CO oxidation. Indeed, in-situ Raman measurements during reduction (CO/N$_2$) and oxidation cycles at 400 °C evidenced the formation of oxygen vacancy clusters in reducing atmosphere, which could reorganize not only in O$_2$ but also upon a temperature decrease, forming isolated vacancies and then evolving in Frenkel and extrinsic oxidized dopant-containing sites when exposed to oxygen.

1. Introduction

In the last decades, mixed oxides have been widely investigated in the field of heterogeneous catalysis, since they represent an attractive alternative to noble metals [1,2]. In particular, cerium oxide has received much attention both as carrier and as oxidation catalyst [3,4]: in fact, numerous studies have been carried out to evaluate the performances of ceria in several applications, including CO oxidation, VOC conversion, diesel soot combustion and low-temperature water gas shift [5–10].

The interesting catalytic activity shown by ceria has been ascribed to its high oxygen storage capacity and its excellent redox properties [11]. However, ceria features depend on several parameters, which can be modified in order to obtain improved active materials. Tuning the synthesis procedure, for example, it is possible to obtain ceria nanoparticles with different morphologies, whose reactivity depends not only on the dimension but also on the crystal planes exposed at their surface [12–16].

Another parameter which plays a crucial role in determining ceria activity is the defect abundancy. Different types of point defects can be found in the ceria lattice, e.g. vacancies or interstitials, and their presence can foster the oxygen transport through the solid matrix [17,18]. Oxygen mobility is an important feature in ceria, since CO oxidation and also other reactions are believed to involve lattice oxygen when they occur on this catalyst. In fact, while heterogeneous catalysis often proceeds via a Langmuir-Hinshelwood mechanism in the case of metal catalysts [19–21], i.e. with the reaction between two species adsorbed at the solid surface, the catalytic pathway usually changes when ceria is used as catalyst or active carrier. For example, mechanisms involving the formation of carbonates or CO disproportionation

1

have been proposed [17,22]. However, most of the authors agree in identifying the main pathway in a Mars-van Krevelen (MvK) type mechanism [4,13,16,19,23]. According to the MvK theory, the reduced reactant is oxidized receiving an oxygen atom from the ceria lattice, while the thus-formed oxygen vacancy will be later on refilled by the oxygen coming from the gas bulk. This mechanism, which has been directly observed by employing labelled oxygen [17], is facet-dependent and is promoted over the highly active (100) facets typical of ceria nanocubes, which present a lower oxygen vacancy formation energy [16].

In order to improve ceria properties, metal dopants can be introduced into the structure, causing lattice distortion and increasing the number of defect sites; as a result, the material can obtain an improved thermal stability accompanied by increased reducibility and oxygen mobility, with beneficial effects on the catalytic activity [6,24–26]. To this end, several elements have been investigated as dopants, and remarkable results were obtained with copper and manganese: in fact, these elements possess different possible oxidation states, and the good coupling of their redox cycles to that of cerium allows to obtain more reducible and active materials [27–31]. In addition, Cu and Mn co-doped systems might benefit from eventual synergetic effects [31]. The doping-induced superficial oxygen vacancies and Ce^{3+} cations can also act as activators for gaseous O_2, whose adsorption on these sites results in the formation of highly-active peroxide or superoxide ions [32]. Furthermore, also the arrangement and distribution of the active sites can affect the final activity [33,34]. Therefore, the cerium reduction-oxidation cycle is directly related to the defect chemistry, and it is promoted on more easily-reducible materials.

Among the different techniques which can be used to investigate ceria-based samples, Raman spectroscopy is of great interest since it is sensitive to the microstructural evolution and defects formation. For these reasons, in situ Raman analyses have been employed in recent years to study ceria defectiveness and to gain new insights into the modification of ceria structure under variable conditions [35–38]. However, though understanding the nature of the defect sites involved in the catalysis is crucial for the rational design of active materials, the identification of the various lattice defects, of their arrangement and of the associated catalytic mechanisms is still under debate.

In the present work, four well characterized ceria-based nanocatalysts [37,39] (consisting of pure ceria nanocubes and ceria doped with 5% Cu, 5% Mn, and 2.5% Cu + 2.5% Mn) prepared via hydrothermal synthesis were used to investigate the role of the defect sites in CO oxidation by Raman spectroscopy. Such reaction was chosen since CO conversion was proved to be directly influenced by the defect abundancy [27,39,40] while the heterogeneous set of catalysts allows to test the behaviour of different defects sites. In situ Raman analyses were performed during the CO oxidation, in order to monitor the evolution of the defects and of the surface chemical species from room temperature (RT) to the catalytic regime. Moreover, the four materials were subjected to cycles of reduction and subsequent oxidation, isolating the vacancy creation and refilling steps in order to better understand how intrinsic and extrinsic defects on ceria-based catalysts are involved in the CO oxidation.

2. Experimental

2.1 Catalysts synthesis

In this study, a set of four different catalysts was considered, consisting of pure ceria nanocubes and ceria doped with 5% Cu, 5% Mn, and 2.5% Cu + 2.5% Mn (named CeO_2, Ce95Cu5, Ce95Mn5 and Ce95Cu2.5Mn2.5, respectively). All the samples were obtained via hydrothermal synthesis, with a procedure reported elsewhere [37,39] adapted from [41]. Briefly, appropriate quantities of $Ce(NO_3)_3 \cdot 6H_2O$ and $Cu(NO_3)_2 \cdot 5H_2O$ or $Mn(NO_3)_2 \cdot 4H_2O$ (all provided by Sigma-Aldrich) were dissolved in 10 ml of deionized water, stirring for some minutes. Meanwhile, another solution was prepared by mixing 48 g of NaOH and 70 ml of deionized water. The nitrate-containing solution was then slowly added dropwise to the hydroxide solution, stirring for 1 h at RT. The mixture thus obtained was then poured into a Teflon liner and placed in an autoclave, which was heated in an oven up to 180 °C for 24 h. Subsequently, the precipitate obtained was rinsed several times with deionized water and ethanol, then it was dried at 60 °C overnight. Finally, the dry powder was gently crushed in a mortar and calcined at 550 °C for 4 h.

2.2 TEM characterization

The morphology and structure of the four different classes of samples were investigated by means of Transmission Electron Microscopy on a FEI Tecnai F20 Super-Twin microscope equipped with a EDAX detector (30 mm^2 active area) for Energy Dispersive X-ray (EDX) Spectroscopy. Concerning sample preparation, the powders were dispersed in high-purity ethanol and subsequently drop-casted on Au holey carbon TEM grids.

2.3 Catalytic performance

Catalytic tests of CO oxidation were carried out to evaluate the activity of the four samples. A fixed bed was prepared inserting 100 mg of catalyst in a quartz U-tube reactor (inner diameter = 4 mm); a K-type thermocouple was placed into the U-tube, with the sensor tip as close as possible to the reactor bed, and the U-tube was housed in a PID-controlled electric furnace. The concentration of CO and CO_2 in the reactor outlet was continuously monitored with a non-dispersive infrared gas analyser (ABB Uras 14). The catalytic bed was initially pretreated for 30 min at 150 °C in a flow of 50 ml/min of air, then it was naturally cooled down to 50 °C in air flow. The test started sending into the reactor a gas mixture containing 1000 ppm of CO and 10% of O_2 in N_2, providing a CO/O_2 ratio typical of diesel exhaust, with a flow rate of 50 ml/min and a GHSV around 40000 1/h. Afterwards, the reactor temperature was increased by 25 °C, and after each increment the reactor was kept isothermal for some time, until a stable signal was shown by the CO and CO_2 analyzer; in this way, adsorption or desorption phenomena are not considered. The test ended when the total CO conversion was achieved. For comparison, a blank test was also carried out with the same procedure, but inserting an inert bed of silica particles in the reactor instead of the catalyst.

2.4 Raman analyses

Raman spectroscopy was employed to investigate the defectiveness of the samples. All Raman analyses were carried out with a Renishaw InVia Reflex micro-Raman spectrometer, equipped with a cooled CCD detector. Excitation was obtained with a solid-state laser emitting at 514.5 nm. The spectra were collected with 32 accumulations lasting 7 seconds each (total acquisition time 224 s), using a 5x objective with a laser power of 10 mW. The spectral resolution was 2 cm^{-1}. The software Renishaw WiRE 3.4 was employed to perform the fitting and deconvolution of the peaks in the vibrational spectra. Three Lorentzian curves were employed to fit the D band of the doped catalysts, setting their initial position at the typical values of Raman shift reported in the literature for the different defect species; the Root Mean Square method was used as optimization algorithm and a baseline correction was performed by the software. When the fitting procedure resulted in a zero-area band, that component was considered absent in the spectrum. The D/F_{2g} value, representative of the defect abundancy, was calculated as the ratio between the area of the deconvolved defect-associated Raman bands (D) and the area of the main vibrational feature of ceria lattice (F_{2g}).

In situ Raman analyses were performed using a Linkam TS1500 cell connected to a temperature controller. A 45-ml/min gas flow was sent into the cell during the tests, in order to expose the sample to the desired atmosphere. To avoid powder displacement during the analyses, catalyst tablets were prepared by compressing some powder into a press, at a pressure of 3 bar. The morphology of the nanopowders was not altered by the procedure (Fig. S1). A small part of a tablet was placed in a tungsten crucible inside the Linkam cell, which was then inserted in the Raman spectrometer.

2.4.1 In situ Raman analyses of the CO oxidation

A constant 45-ml/min flow of a gas mixture containing 1000 ppm of CO and 10% O_2 in N_2 was sent into the cell during these analyses, employing Brooks 5850S mass flow controllers. After having acquired a spectrum at RT (RT_i), the cell was heated with a constant rate of 3 °C/min up to 500 °C, recording spectra at different temperatures. After collecting a spectrum at 500 °C, a 45-ml/min flow of air (20% O_2 in N_2) was sent into the cell, and after 10 min the cell was cooled down to RT. Finally, a last spectrum was acquired at RT ($RT_{cool.}$).

A 45-ml/min flow of pure N_2 was sent into the cell before collecting a spectrum at RT (RT_i). Then the cell was heated up to 400 °C with a rate of 10 °C/min. After waiting some minutes for the stabilization of the temperature, a first spectrum was collected in nitrogen atmosphere. Then, different gaseous mixtures were sent into the cell, changing the gas composition every 40 min. First 1000 ppm of CO in N_2 were flowed, followed by flushing the cell with pure N_2 and finally sending O_2. After flushing the cell with nitrogen again, a second cycle of reduction in CO/N_2 atmosphere, flushing in N_2 and reoxidation in O_2 was repeated. Since the gas requires about 10 min to completely replace the previous atmosphere in the cell, Raman spectra were acquired after 10, 25 and 40 min from each change of the gas composition. Finally, pure N_2 was sent into the cell, which was then cooled down to RT, and a last spectrum was collected at RT ($RT_{cool.}$). In order to analyze the kinetic of defect evolution on the Ce95Cu5 catalyst, time series were acquired during the first ten minutes after the gas change. Raman spectra were recorded continuously, at the conditions specified previously except for the total acquisition time that was set to 15 s.

3. Results and Discussion

3.1 Catalyst characterization and activity

A set of four different catalysts was considered in this study, consisting of pure ceria (named CeO_2) and ceria doped with 5% Cu (Ce95Cu5), 5% Mn (Ce95Mn5), and 2.5% Cu together with 2.5% Mn (Ce95Cu2.5Mn2.5). These four materials, obtained via hydrothermal synthesis, were extensively characterized with complementary techniques, such as X-ray diffraction (XRD), nitrogen physisorption, field emission scanning electron microscopy (FESEM), and X-ray photoelectron spectroscopy (XPS), as reported elsewhere [39]. Some of the physico-chemical and textural properties revealed by these analyses are resumed in Table 1.

Transmission Electron Microscopy (TEM) was carried out in order to further investigate the morphology and structure of the four classes of samples; Fig. 1 provides an overview of significant results.

Concerning the pristine CeO_2 nanostructures, they exhibit the usual nanocube morphology, with typical lateral size in the range (500 nm ÷ 20 nm), in accordance with previously reported results [39]. Selected area electron diffraction (SAED) provided in the Supporting Information confirms that the sole crystalline phase present is CeO_2 (face-centered (F) lattice, Fm-3m space group [42]). As expected, High-resolution TEM (HRTEM) and subsequent analysis of Fast Fourier Transforms (FFT) of the images suggest that the nanocubes of different size are single crystals, showing interplanar spacings in accordance with CeO_2 structure (see Table S1).

Regarding the doped samples, it is clear by comparison of low-magnification TEM images that the presence of the different nitrate precursors influences the morphology of the powders. Specifically, the synthesis of Ce95Cu5 and Ce95Cu2.5Mn2.5 provides nanoparticles with diameter values approximately in the (30 nm ÷ 5 nm) range, while Ce95Mn5 exhibits the presence of both nanoparticles (30 nm ÷ 5 nm) and nanocubes (lateral size 200 nm ÷ 20 nm). Regarding the crystalline structure, SAED patterns (Fig. S2) confirm the presence of CeO_2 with no significant distortion of the unit cell and the absence of secondary phases. These results are in accordance with the information obtained by HRTEM, showing that the doped nanostructures are single crystals regardless of the particular morphology, and with the XRD analyses (Fig. S3). Moreover, the presence of the doping elements in the samples was confirmed by Energy Dispersive X-ray (EDX) spectroscopy (representative spectra are provided in Fig. S4).
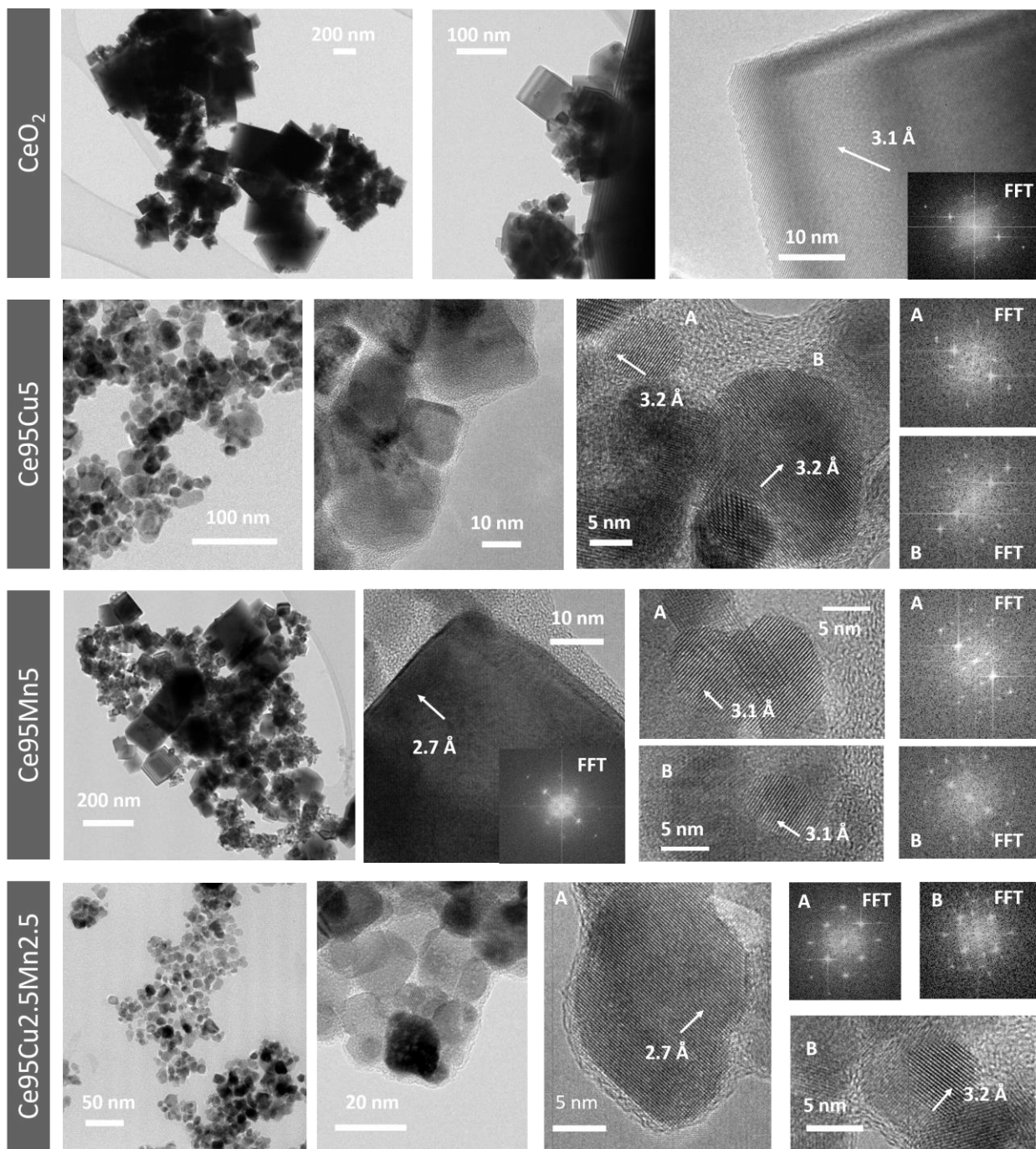
Fig. 1. TEM characterization of the pristine and doped ceria powders, providing Bright-Field low magnification images and High-Resolution TEM images with corresponding Fast Fourier Transforms (FFT). In HRTEM images, interplanar spacings calculated from FFT are provided (~3.1 Å (111), ~2.7 Å (200) family of planes of the CeO_2 structure). Labels A and B mark the correspondence between the analyzed particle and its FFT.

The results of the catalytic activity test towards CO oxidation are recalled in Fig. 2 [39]. The graph shows the CO conversion as a function of the temperature over the four samples, compared to the non-catalytic CO oxidation (yellow curve), promoted only by the temperature. All the catalysts are able to significantly reduce the temperature required for the CO oxidation, but a considerable difference can be noticed between pure and doped ceria in terms of performances. For a quantitative comparison, the specific reaction rate of CO oxidation (r_{CO}) can be considered, namely the rate of CO conversion at a given temperature normalized to the specific surface area of the catalyst. The values calculated at 120 and 150 °C are reported in Table 1: while pure CeO_2 showed a low r_{CO}, this parameter was remarkably higher for the three doped materials. In fact, Ce95Mn5 exhibited a specific reactivity ten times higher already at 120 °C, while even

better results were obtained with Ce95Cu2.5Mn2.5 and Ce95Cu5. The higher activity of the Cu-doped samples is related to their higher specific surface area and reducibility [39], but it also depends on a higher defect abundancy [37]. Indeed, since the CO oxidation is believed to occur via a Mars-van Krevelen type mechanism on ceria-based materials, oxygen vacancies and lattice defects are directly involved in the catalysis.
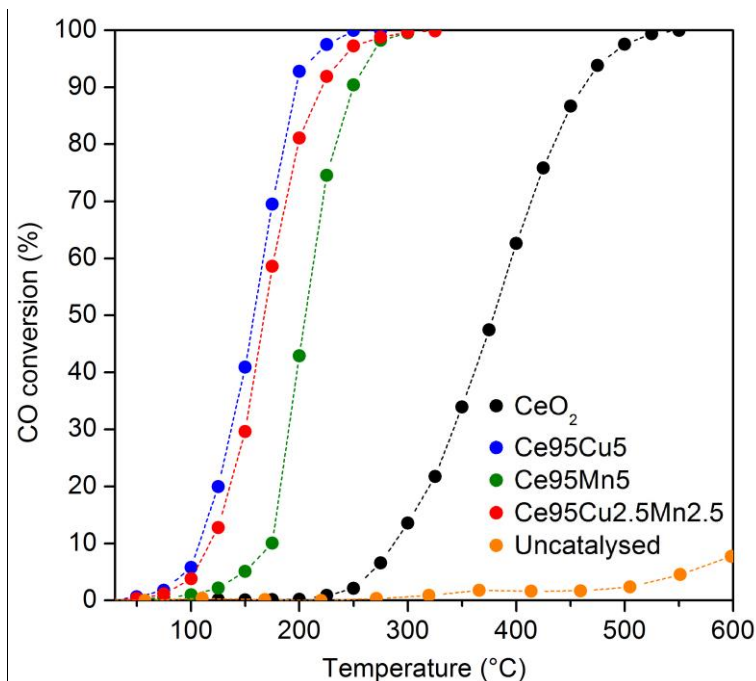

Fig. 2. CO conversion curves as a function of the temperature, obtained feeding the reactor with a gas mixture containing 1000 ppm of CO and 10% of O_2 in N_2 (detailed catalysts activity assessment, except for Ce95Mn5, reported in [39]).

Table 1

Structural, physico-chemical and catalytic properties of the four samples.

Catalyst	D_C [a] [nm]	a [a] [Å]	SSA [b] [$m^2 g^{-1}$]	Ce^{3+} [c] [%]	D/F_{2g} [d]	r_{CO} at 125 °C [e] [$\mu mol_{CO}\ h^{-1}\ m^{-2}$]	$T_{50\%}$ [e] [°C]
CeO_2	135	5.412	9	21	0.022	0.17	379
Ce95Cu5	34	5.409	46	27	0.256	5.33	158
Ce95Mn5	79	5.409	17	21	0.124	1.57	206
Ce95Cu2.5Mn2.5	23	5.408	52	26	0.231	3.02	168

[a] Average crystallite size (D_C) and lattice constant (a) estimated via XRD [37]

[b] Specific surface area (SSA) obtained via N_2-physisorption [37]

[c] Superficial Ce^{3+} abundancy evaluated via XPS [37]

[d] D/F_{2g} ratio obtained from the Raman spectra collected at RT [37]

[e] Temperature at which the 50% of CO conversion was reached ($T_{50\%}$) and specific reaction rate of CO oxidation (r_{CO}) at 125 °C estimated from the CO oxidation tests

Raman spectroscopy is a valuable tool that can be fruitfully employed in the investigation of ceria defectiveness [37,43,44]. Indeed, besides the main F_{2g} peak located at $460 - 465$ cm^{-1}, ascribed to the symmetric stretching mode of the Ce–O bonds [18,36], a band related to the presence of defects can be observed at higher shift in a typical Raman

spectrum of ceria. Usually, a single recognizable component can be detected around 595 cm^{-1} on pure ceria: this D1 peak can be linked to the presence of Frenkel-type defects, in which a vacancy is generated by the displacement of an oxygen atom into an interstitial position [36,45,46]. Besides this component, other peaks can appear in the defect region of the spectra recorded on doped ceria, due to the formation of other types of defects: these sites can be considered extrinsic, i.e. induced by the doping, in contrast with the intrinsic Frenkel pairs already present in pure ceria.

When the four samples investigated in this study are concerned, the three doped samples were indeed characterized by the presence of a more intense and broader defect band in their Raman spectra with respect to pure ceria [37], as expected due to the good dispersion of the dopants in ceria lattice suggested by the absence of segregated secondary phases. Following a well-established method for comparing the defect abundancy of different ceria-based samples in a semi-quantitative way [12,40,46,47], the ratio between the area of the D band and that of the F_{2g} peak (D/F_{2g}) was calculated (see Table 1). Although it was previously observed that nanocubes are characterized by an increased D band contribution compared to nanopolyhedra [46], due to the exposure of more reactive (100) facets, in this case the influence of dopant incorporation in ceria lattice clearly overcomes any shape-related effect. In detail, for the four catalysts the D/F_{2g} ratios calculated at RT followed the trend CeO_2 < Ce95Mn5 < Ce95Cu2.5Mn2.5 < Ce95Cu5, which well correlates with the catalytic activity towards CO oxidation discussed above [37]. As shown by the representative spectra deconvolution of CeO_2 and Ce95Cu5 in Fig. 3, the higher D/F_{2g} ratio for the doped catalysts is accounted for by an increase of the D1 peak contribution, that indicates a doping-induced rise of the abundancy of Frenkel-type sites, as well as by the appearance of a D2 band, located above 600 cm^{-1}, that can be ascribed to oxidized sites with a dopant cation not containing oxygen vacancies [37,48–50]. Finally, a D3 component, located around 550-570 cm^{-1}, usually assigned to oxygen vacancies [18,51–53], was barely detectable only in the spectra of the two Cu-doped materials (schematic structures of the three defect types are displayed in Fig. S5).

As a matter of fact, Raman spectroscopy has a great potential in probing the real time evolution of the different defect sites and is expected to provide new details on their involvement in the reaction mechanism; for this reason, in situ Raman analyses were performed studying the catalysts under reactive conditions.
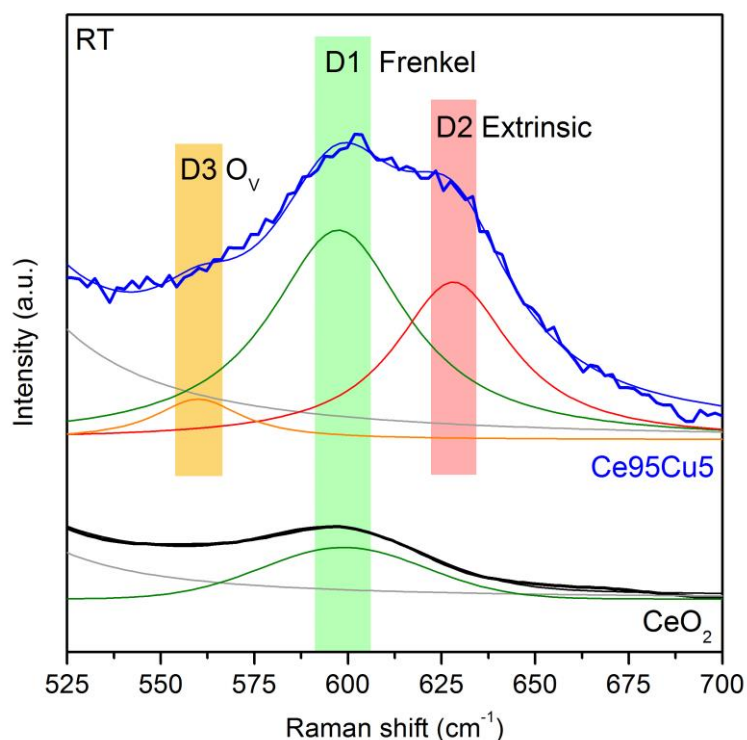

Fig. 3. Magnification of the defect region of the Raman spectra collected in air at RT on the CeO_2 and Ce95Cu5 samples. The spectra were normalized to the F_{2g} peak intensity and are vertically shifted for clarity reason. The curves obtained by the fitting and deconvolution of the defect band are reported as thin lines.

3.2 In situ Raman analyses of the CO oxidation reaction

In order to provide new insights into the catalytic role played by the defects, Raman measurements were carried out during the CO oxidation. A mixture containing 1000 ppm of CO and 10% of O_2 in N_2 was flowed on the catalyst, then the sample was heated and Raman spectra were collected at different temperatures. No changes were observed at RT upon the exposure of the samples to CO.

Fig. 4A reports the Raman spectra acquired on the CeO_2 sample. As discussed above, the defect band consisted in a single D1 peak, as displayed in Fig. 3, and the evolution of this component during the test is reported in the inset of Fig. 4A. As the temperature rose, the peaks in the spectra moved to lower Raman shift and became broader: the red-shift is a consequence of the thermal-induced strain, while the peak broadening is mainly due to anharmonicity effects [48,54]. In agreement with the recent literature for temperature-dependent Raman analyses on ceria catalysts [37], a foreseen growth of the D3 band as a consequence of the reduction of the catalyst could not be identified since its contribution would be masked by these spectral changes. A continuous decrease of the intensity of the bands was also reported previously during heating ramps in air [37]. Instead, in the case of CO oxidation a clear inversion of the trend was noticed at around 300 °C.
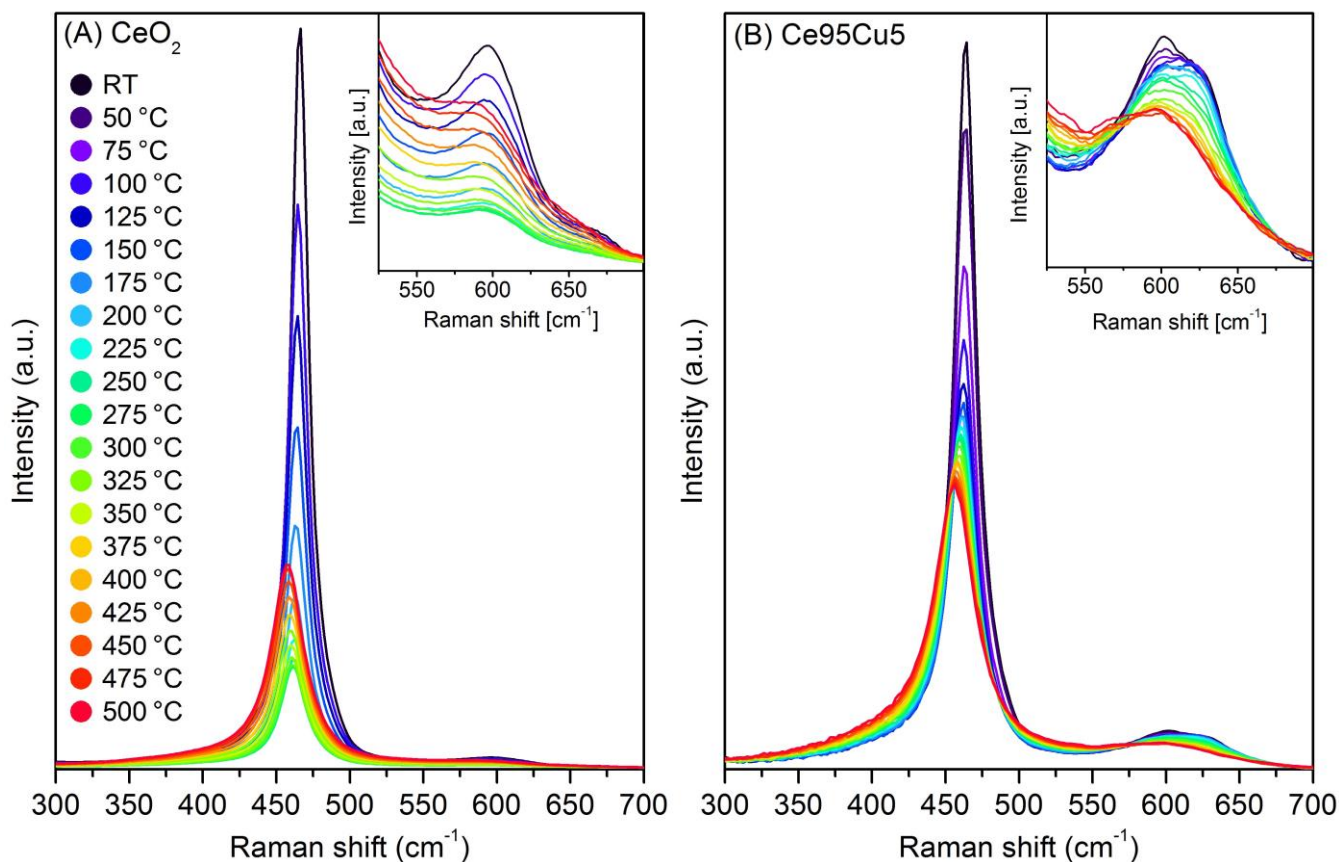

Fig. 4. Raman spectra collected at different temperatures during the CO oxidation (1000 ppm of CO and 10% of O_2 in N_2) on the CeO_2 (A) and Ce95Cu5 (B) samples. The defect region is magnified in the insets.

To better understand the origin of this unexpected behaviour, the main curve parameters of the F_{2g} bands were analyzed as a function of the temperature and compared with the analogous parameters obtained heating the sample in air (tests reported in [37]). Position and width of the F_{2g} peak changed almost linearly with the temperature in presence of CO, with a very similar trend to that observed performing the analyses in air (see Fig. S6). On the other hand, the F_{2g} band showed a sharper intensity decrease in the low temperature range (RT – 250 °C) with respect to the sample heated in air (see Fig. 5C), followed by an almost stationary phase (250 °C – 300 °C) and a net and continuous growth above 300 °C. The discussed behaviour is consistent with an intensity increase caused by a change of the optical absorption by the catalyst, and thus of the laser beam penetration depth. Indeed, defect formation, topological evolution yielded by structural distortions or other similar effects would imply a modification of the vibrational band shape involving also the width and the spectral position. A deeper inspection of the spectra reveals that this behaviour seems to be connected to that of another band, located around 1500 cm⁻¹; a magnification of this region of the Raman spectra is reported in Fig. 5A. As displayed in the picture, at RT a low-intensity broad band was detected at 1535 cm⁻¹: this Raman feature can be associated to the presence of some organic contamination on the sample surface, since it

8

disappeared completely during the heating. At the same time, as the temperature rose, a structured band appeared in the Raman spectra; one narrow component, located at 1510 cm^{-1}, could be observed already at 100 °C, then a second peak near 1500 cm^{-1} could be distinguished with respect to the first one starting from 200 °C, and finally a shoulder appeared at around 1525 cm^{-1} above 300 °C. Despite the general decrease in the Raman intensity, this band grew until 300 °C, then its intensity decreased. This suggests the assignment of the multi-component band to carbon-based molecules forming on the nanoparticle surface, which are later desorbed and oxidized by the catalyst at high temperature. An analogous behaviour could be noticed also for a weaker band around 1120 cm^{-1} (see Fig. S7 A), that appears superimposed to the second order mode of ceria and can be reasonably assigned to the vibrational pattern of the same chemical species. The formation of these compounds does not seem to be related to the presence of previous carbonaceous contamination, since very similar results were obtained when repeating the in situ Raman measurements on a CeO_2 sample pretreated in air at 500 °C for 1 h (see Fig. S8). Furthermore, Raman spectra collected through faster acquisitions and focusing the spot in different zones of the sample allowed to rule out that laser-induced effects could account for the generation of the observed compounds.
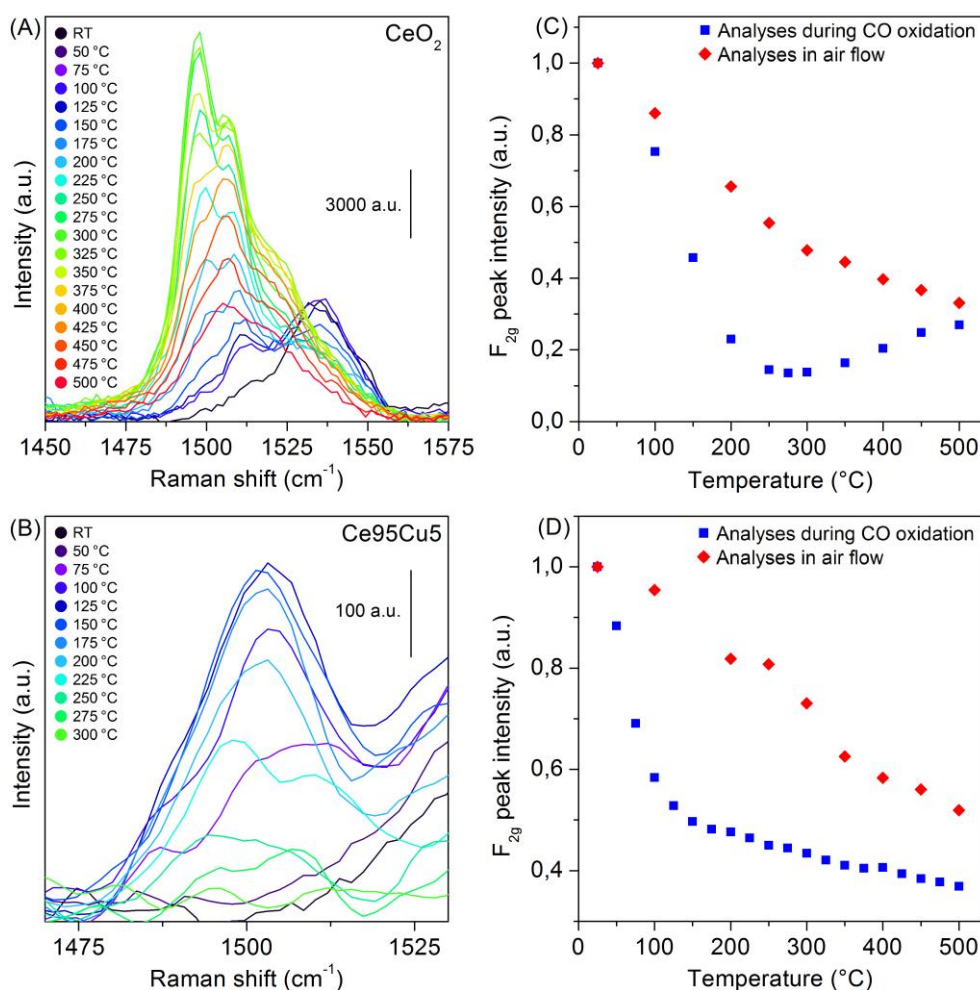

Fig. 5. Magnifications in the 1450-1575 cm^{-1} range of the Raman spectra collected at different temperatures during the CO oxidation (1000 ppm of CO and 10% of O_2 in N_2) on the CeO_2 (A) and Ce95Cu5 (B) samples. Height of the F_{2g} peak as a function of the temperature in the spectra recorded on the CeO_2 (C) and Ce95Cu5 (D) samples during the in-situ analyses of CO oxidation (spectra reported in Fig. 4 A and B) and during the analyses in air flow (spectra reported in [37]); the values were normalized to the height measured at RT.

Despite the formation of carbonates or formates, resulting from the interaction of CO with ceria, has been previously observed by FTIR spectroscopy during CO conversion [55,56], the typical vibrational modes of such species are not consistent with the Raman fingerprint detected in the in situ analyses here reported. Instead, this pattern closely resembles the Raman spectra of polyenes, which are featured by two main bands related to single and double carbon-carbon bond stretching, respectively [57]. The position of such bands varies with the length of the polyene chain [57,58], possibly explaining the presence of different components. Moreover, the conjugated system of polyenes may be characterized by electronic transitions around 500 nm for specific chain lengths [57], leading to the absorption of part of

the excitation/scattered light, causing the decrease of the Raman signal intensity of ceria. Above 300 °C, however, the CeO_2 catalyst starts to be significantly active, as shown in Fig. 2; the subsequent growth of the intensity of ceria-related bands could be therefore a consequence of the disappearance of the adsorbed species revealed by the 1500 cm^{-1} and 1120 cm^{-1} bands. It should be noted that the matching between the excitation wavelength and the electronic transition of the analyzed molecules is responsible for a resonance Raman regime which can lead to the observed strong enhancement of the Raman scattering efficiencies. For this reason, the formation of different hydrocarbons, including the resonant polyenes, can be hypothesized during the first stages of the CO oxidation reaction, as a consequence of a dissociative adsorption of CO on the catalyst surface together with an involvement of the initially present OH groups.

Fig. 4B reports the spectra acquired performing the in-situ analysis of CO oxidation on the Ce95Cu5 sample. As previously discussed, three convoluted peaks were observed in the defect band of this material, as shown in the RT spectrum reported in Fig. 3; the evolution of this band during the test is magnified in the inset of Fig. 4B. Again, it was not possible to distinguish between catalyst reduction and the always present thermally induced red-shift and broadening of the D band components. Fig. 4B shows that the spectral intensity decreased monotonically while heating the cell, maintaining the behaviour also at high temperature. However, this variation was characterized by two different slopes in different temperature ranges.

The values of the F_{2g} peak position, width and height calculated from the spectra presented in Fig. 4B were compared with the analogous parameters obtained heating the same sample in air (tests reported in [37]). In analogy with the results obtained for pure ceria, the changes in position and width were linear and very similar during the two different tests (see Fig. S9). Instead, the intensity drop was faster in the early heating phase when flowing CO, as displayed in Fig. 5D, then it became slower and constant above 150 °C. Again, this behaviour is probably associated to that of the band detected at 1500 cm^{-1}, whose magnification is reported in Fig. 5B. Despite the spectra collected on Ce95Cu5 are noisier, a distinguishable peak appeared at 75 °C, reached the maximum intensity at 125 °C and then decreased until disappearing above 225 °C. Again, a band around 1120 cm^{-1} followed the same trend with the temperature (see Fig. S7 B). These bands could be attributed to the formation of polyenes on the catalyst surface, which could absorb visible light, thus weakening the Raman spectral intensity. Above 125 °C, however, when the catalytic activity of the Ce95Cu5 sample starts to be significant, the adsorbed carbonaceous species are oxidized. The temperature at which the 1500 and 1120 cm^{-1} bands reach their maximum seems thereby to be correlated with the catalytic activity. Since the light off temperature of Cu-doped ceria is lower than that of pure CeO_2, a lower amount of molecules can be expected to form on the surface; as a result, the effect of the decreasing light absorption associated to the polyenes conversion only partially mitigates the drop of the spectral intensity caused by the heating.

Concerning the spectra collected on the two Mn-doped catalysts (reported in Fig. S10), a monotonic decrease of the F_{2g} intensity was observed during the heating, which was however very slight for Ce95Mn5. For both these samples, no clear band was detected at 1500 cm^{-1}. Several reasons can account for its absence, including the higher noise associated with the higher light absorption of the catalysts [37], the formation of shorter/longer polyenes which do not experience a resonant Raman enhancement at 514.5 nm or a minor amount of residual OH species.

The Raman analysis therefore allows to identify an unusual reaction pathway, which probably accounts for a minor fraction of the total CO conversion, but supports the existence of CO dissociative adsorption in an O_2-containing atmosphere. A similar disproportionation mechanism on ceria was in fact previously observed only in reducing conditions leading to the growth of soot-like amorphous carbon on the catalyst surface [17,59]. Hence, the presence of strongly active sites, needed to lower the high energy barrier to the CO bond dissociation [60], can be hypothesized.

After reaching 500 °C, the samples were cooled down to RT in air flow and a spectrum was acquired ($RT_{cool.}$), which can be compared with the one collected at RT at the beginning of the test (RT_i). Comparisons between these two spectra for the four catalysts are reported in Fig. 6. For pure ceria, the two spectra are almost completely overlapped, and the total reversibility indicates that the CO oxidation does not significantly affect the structure of the catalyst. Instead, for the three doped samples some differences were detected in the defect region, as displayed in the insets of Fig. 6. The growth in the intensity of the defect band suggests that new defects were formed in the samples while the reaction occurred. This behaviour is quite unusual, since reversibility of the Raman spectra or a decrease of the defect band intensity after thermal cycles have been typically reported in the literature [12,48,61]. However, a raise in the defect band was already noticed in a previous study on the same set of catalysts [37], but only for the Ce95Cu5 sample. Instead, this time an increase in the defectiveness is evident also for Ce95Mn5, though slight, and Ce95Cu2.5Mn2.5. The Ce95Cu5 catalyst exhibited the highest increase in the D/F_{2g} ratio among the tested materials, with a variation of

this parameter higher than that previously observed after a thermal cycle in air (+52% instead of +16%) [37]. Also the Ce95Cu2.5Mn2.5 sample underwent a significant increase in the defectiveness, while the variation was less marked for Ce95Mn5. The microstructure of all the doped catalysts is therefore significantly affected by the CO oxidation reaction.
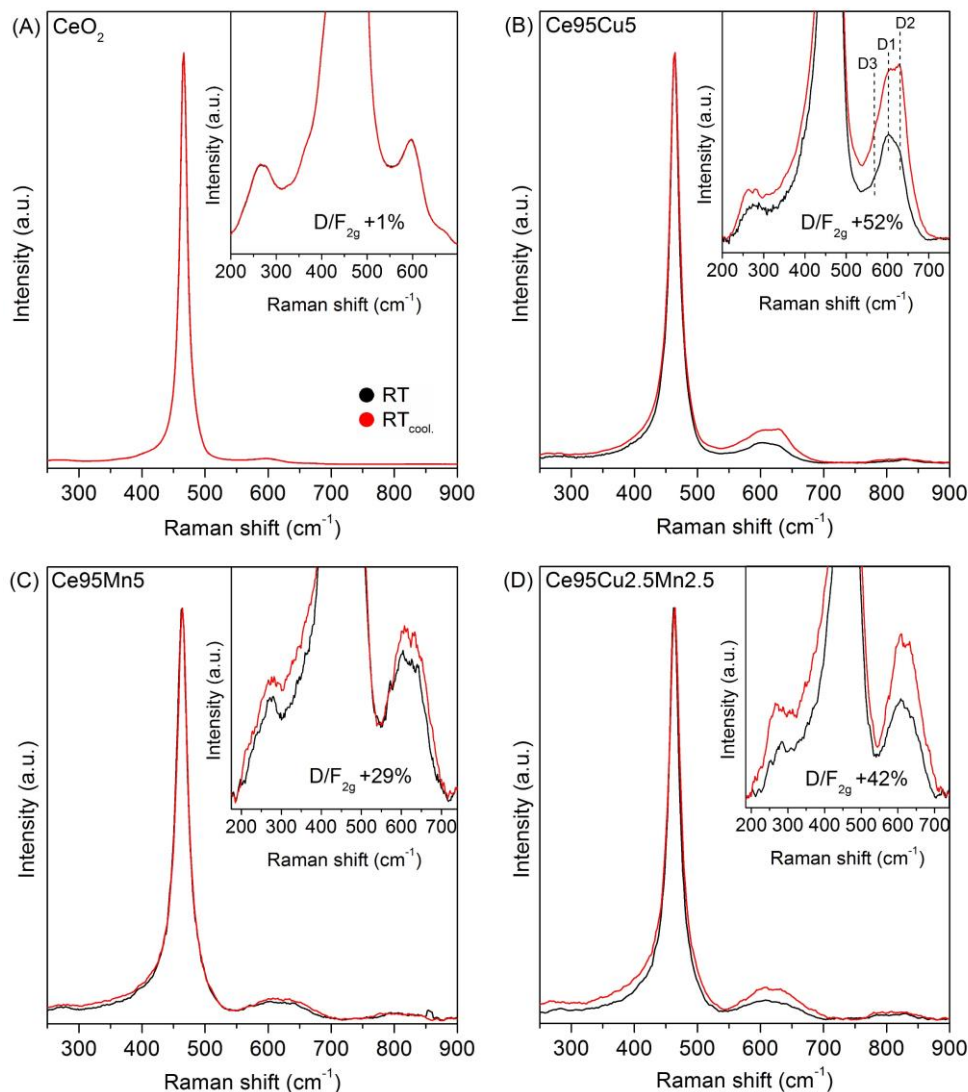

Fig. 6. Comparisons between the Raman spectra acquired in air at RT at the beginning (RT_i) and at the end ($RT_{cool.}$) of the in-situ analyses performed during CO oxidation on the CeO_2 (A), Ce95Cu5 (B), Ce95Mn5 (C) and Ce95Cu2.5Mn2.5 (D) samples. In each inset, a magnification of the defect band is shown, and the increase of the D/F_{2g} ratio after the test is reported. The spectra were normalized to the intensity of the F_{2g} peak.

3.3 In situ Raman analyses during reduction-oxidation cycles

In order to further investigate the structural changes induced in ceria-based materials by the interaction with CO, Raman analyses were performed exposing the catalysts to cycles of reduction and oxidation, following the schedule reported in Fig. 7. The samples were heated in pure N_2 until 400 °C, since all the four catalysts are active towards CO oxidation at this temperature. Raman spectra were collected 10, 25 and 40 min after each gas change. After keeping the catalysts in an atmosphere of 1000 ppm of CO in N_2, pure nitrogen was used to flush the cell; afterwards, the samples were reoxidized in O_2. Finally, after cleaning the cell with nitrogen, a second cycle of reduction and oxidation was carried out, to verify if the changes observed in the spectra were reproducible. Unfortunately, the evolution of the surface oxygen species could not be monitored, since no variations were detected in the regions in which the typical bands of peroxide or superoxide ions can be found.

The Raman spectra collected during the cycles on pure CeO_2 after 40 min from each atmosphere change are presented in Fig. 8A. In the inset, the defect bands normalized to the F_{2g} peak are magnified. No significant spectral variations were detected when changing the gas composition, confirming the CeO_2 structural stability discussed above.
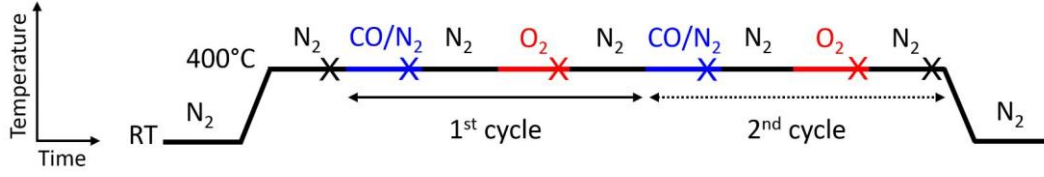

Fig. 7. Experimental scheme for the in-situ Raman analyses performed during cycles of reduction and oxidation. The crosses indicate when the spectra reported in Fig. 8 were collected.
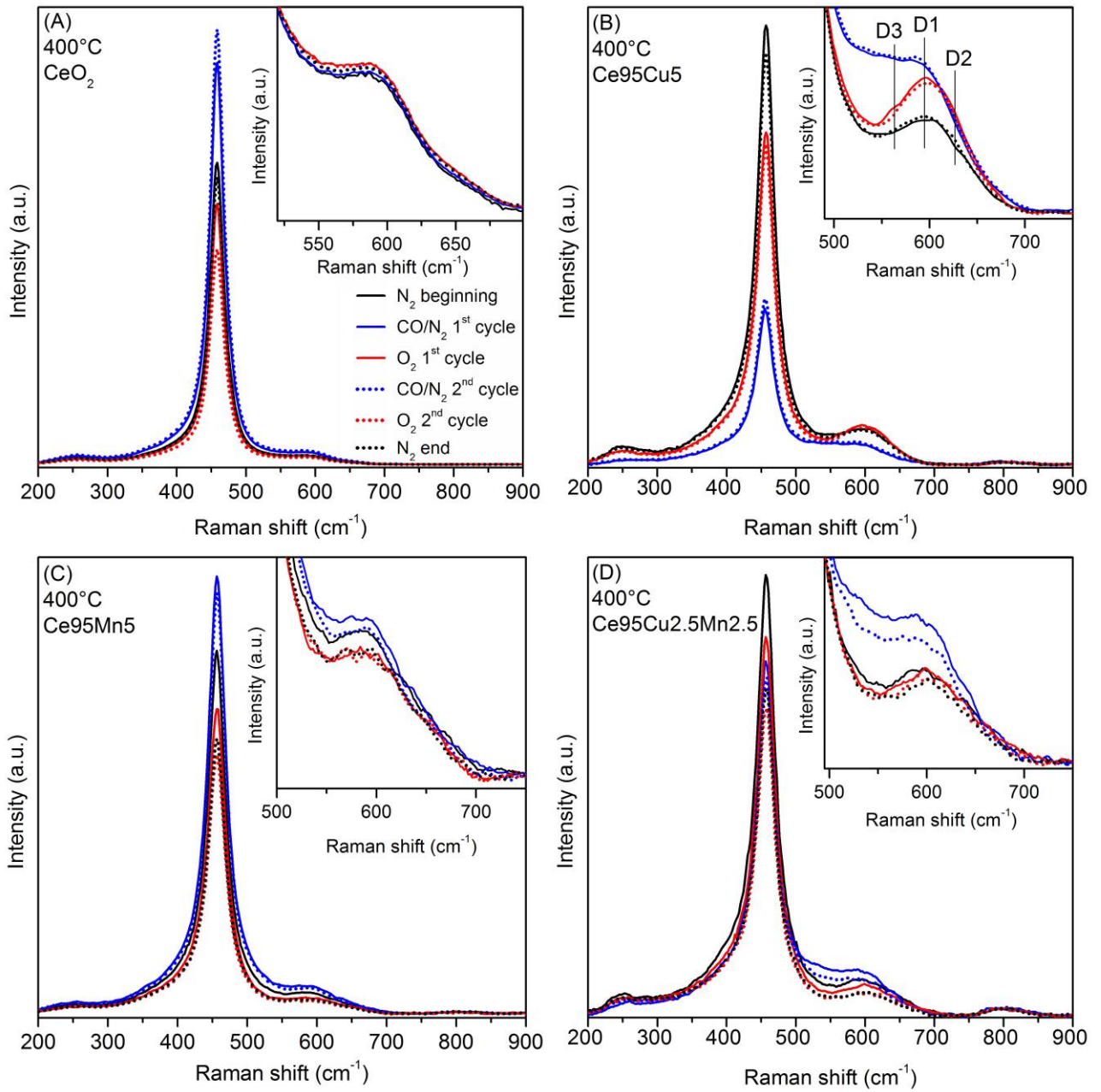

Fig. 8. Raman spectra acquired during cycles of reduction (1000 ppm of CO in N_2) and oxidation (pure O_2) at 400 °C on the CeO_2 (A), Ce95Cu5 (B), Ce95Mn5 (C) and Ce95Cu2.5Mn2.5 (D) samples. The spectra were collected 40 min

after the gas change, in correspondence with the crosses in Fig. 7. The spectra recorded during the first cycle are represented with solid lines, while the spectra measured during the second cycle are depicted with dotted lines. In each inset, a magnification of the defect region of the spectra normalized to the intensity of the F_{2g} peak is reported.

Conversely, remarkable differences were observed among the spectra acquired on the Ce95Cu5 sample in the different atmospheres, which are displayed in Fig. 8B. A drastic decrease in the spectral intensity was observed under reducing conditions; moreover, this event was coupled with a broadening of the F_{2g} peak and a variation of the defect band, as detailed in the inset of Fig. 8B (the normalized spectra are reported for a more proper comparison). In fact, after flowing CO in N_2, the defect band acquired a flat shape, due to the rise of a component located around 550 cm^{-1}; however, the absolute intensity change of the different defect bands could not be evaluated due to the simultaneous spectral intensity drop, that could lead to unreliable conclusions.

As anticipated, a D3 peak lying in the 530-560 cm^{-1} spectral region is usually ascribed to the presence of oxygen vacancies, whose formation is associated to the reduction of Ce^{4+} to Ce^{3+} [18,38,46,53]. A similar effect was already observed by Agarwal et al. [36] and Wu et al. [46], when collecting UV Raman spectra on ceria nanorods after flowing highly concentrated CO (33% in He) at 350°C and hydrogen, respectively. Moreover, Andriopoulou et al. reported a flattening of the Raman defect band of rare-earth doped ceria-zirconia in reducing conditions [48]. Actually, Agarwal et al. also noticed the contemporary formation of carbonates and formates adsorbed on the catalyst surface by FTIR spectroscopy, but only a minor part of the newly-generated defects was ascribed to the presence of these carbonaceous species. Furthermore, they suggested that the broad band at 550 cm^{-1} could result from the contribution of different components: besides simple oxygen vacancies, other types of defects may form during CO exposure, e.g. interstitial sites and Schottky disorders; at the same time, vacancy clustering may occur, resulting in the formation of dimers or trimers [36] which are likely to give rise to Raman signals slightly different from that of the isolated defects.

A similar explanation can be given also for the Ce95Cu5 sample analyzed in this study, which appears to be more reducible than nanostructured pure ceria: the appearance of a broad D3 band can indicate the formation of new defectiveness at quite low CO concentrations, and the induced lattice strain can account for the F_{2g} broadening and for the dramatic intensity drop in the spectrum [62]. Indeed, the deposition of carbon at the catalyst surface, that could cause an increased absorption and thus a reduced Raman intensity, was not observed, probably due to the quite high temperature compared to the light off of Ce95Cu5 (see Fig. S11). However, a partial recovery of the spectral intensity was obtained sending O_2 into the cell; at the same time, the intense and broad D3 band observed in CO atmosphere completely vanished when the sample was reoxidized, while a growth of the D1 and D2 peaks was noticed. This suggests that the refill of the oxygen vacancies can occur at 400 °C in pure oxygen atmosphere, and it is concomitant with the formation of new Frenkel pairs and extrinsic oxidized defect sites. The results obtained performing the second cycle of reduction and oxidation were almost the same; furthermore, the spectrum acquired in N_2 at the end of the test is very similar to that collected at the beginning in the same atmosphere, both considering the spectral intensity and the D band. Therefore, eventual irreversible structural changes induced by reduction or oxidation cannot be noticed at 400 °C.

Fig. 8C displays the spectra collected on the Ce95Mn5 sample. The spectra acquired in the different atmospheres present only minor variations in the D band, which is slightly more intense and is probably featured by the appearance of a weak D3 component in reducing conditions; when O_2 is flowed, instead, the defect band becomes a little less intense than that of the spectrum measured in nitrogen at the beginning: this variation suggests that all the oxygen vacancies previously created in reducing atmosphere can be completely refilled, while not all of the initial Frenkel and extrinsic D2 defects are restored during the reoxidation phase. The D band growth is less marked during the second exposure to CO, showing that the reduction is more difficult after the first cycle; moreover, the final spectrum in nitrogen is similar to those recorded in O_2. The non-complete reversibility of the behaviour of this catalyst could be associated to the formation of carbonates or formates at the surface, that may reduce the activity during the second cycle [55]. However, due to the low sensitivity of Raman spectroscopy towards C-O bonds and to the low concentration of CO, carbonate and formate groups were not detected in the spectra.

An intermediate behaviour was noticed for the Ce95Cu2.5Mn2.5 sample, whose spectra are reported in Fig. 8D. In reducing conditions, a remarkable rise in the D band can be noticed, especially around 550 cm^{-1}, as happened for Ce95Cu5. Moreover, a red-shift and a broadening of the F_{2g} peak were detected, coupled with a decrease in the spectral intensity. All these effects can be due to the generation of new defect sites during CO exposure. However, similarly to the Ce95Mn5 sample, Ce95Cu2.5Mn2.5 spectra acquired in nitrogen and oxygen during the second cycle are very

similar, while a less marked rise in the D band was noticed during the second reduction; furthermore, the changes observed in this phase occurred gradually, as pointed out in Fig. S12, while all the spectral changes were already complete 10 minutes after the gas change for the other samples. These results suggest that the newly-formed oxygen vacancies can be easily refilled by O_2; however, the behaviour of the material is not totally reversible, since after a complete oxidation the formation of D3 defects in reducing atmosphere seems to be partially hindered.

After the cycles of reduction and oxidation at 400°C, Raman measurements were carried out on the different samples cooled to RT; the collected spectra ($RT_{cool.}$) are reported in Fig. 9, together with those acquired in the same conditions before the test (RT_i). An almost total reversibility was confirmed for pure CeO_2, since only negligible differences can be noticed between the spectra in Fig. 9A. Also the Ce95Mn5 sample exhibited only minor variations, limited to a slight displacement of the defect band towards higher Raman shift, probably induced by the oxidation. Conversely, a remarkable growth of the D band after the test was observed for the two Cu-doped samples. Actually, the ternary oxide experienced an intermediate increase in the D/F_{2g} ratio, similar to that previously observed after the CO oxidation. The Ce95Cu5 catalyst, instead, underwent a higher rise in the D band after the cycles of reduction and oxidation, as displayed in the inset of Fig. 9B. The exposure of this sample to different atmospheres seems thereby to produce significant changes in the microstructure, fostering the increase in the defectiveness.
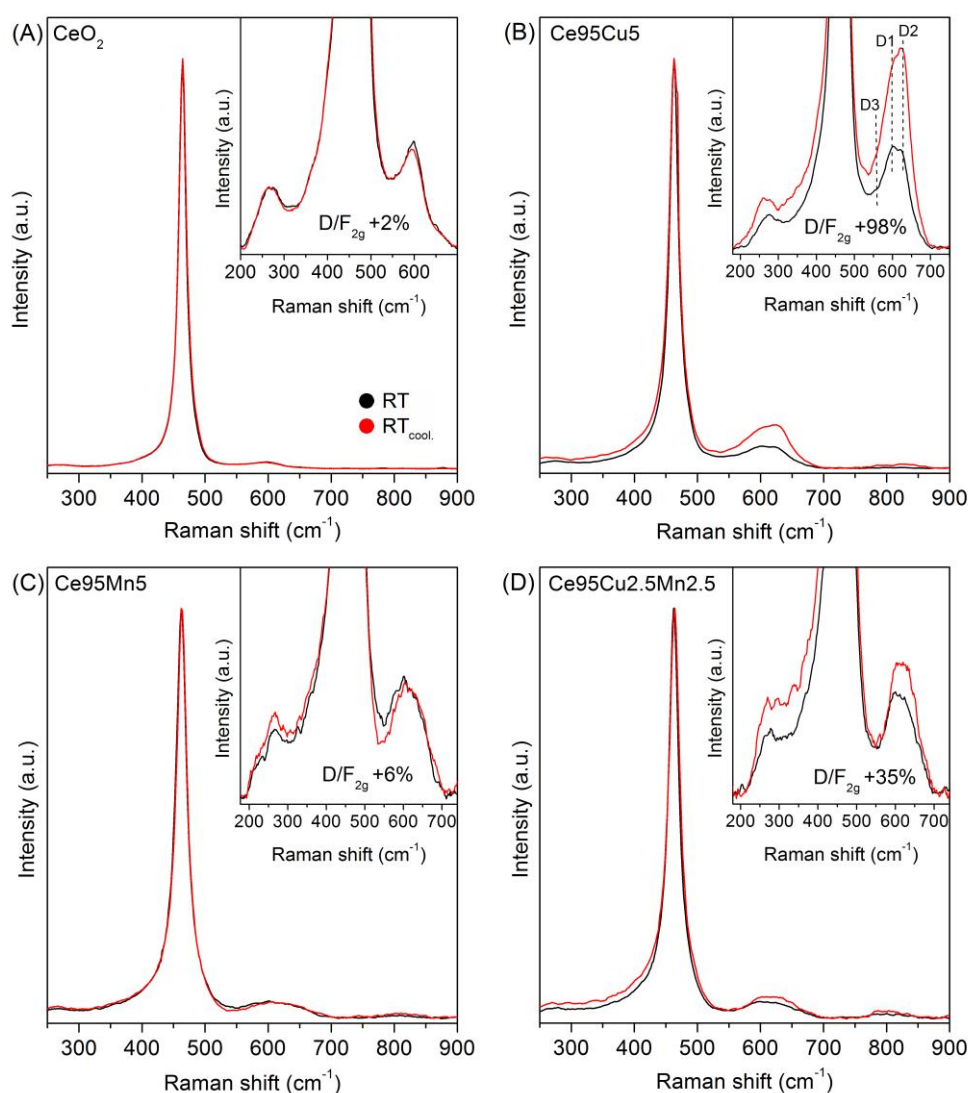

Fig. 9. Comparisons between the Raman spectra acquired in air at RT at the beginning (RT_i) and at the end ($RT_{cool.}$) of the in-situ analyses performed during cycles of reduction and oxidation on the CeO_2 (A), Ce95Cu5 (B), Ce95Mn5 (C) and Ce95Cu2.5Mn2.5 (D) samples. In each inset, a magnification of the defect band is shown, and the increase of the D/F_{2g} ratio after the test is reported. The spectra were normalized to the intensity of the F_{2g} peak.

A correlation can be found between the behaviour of the four materials during the Raman analyses and their catalytic activity. Actually, the Ce95Cu5 sample, which was found to be the most reducible and performing catalyst, exhibited the most remarkable increase in the D3 band in reducing conditions, in addition to the highest increase in the D/F_{2g} ratio after the test. Minor changes were detected in the spectra collected on the Ce95Mn5 sample, which in fact showed a less interesting catalytic performance. For the ternary oxide, an intermediate behaviour between those of the Cu- and Mn-doped samples corresponded to an intermediate activity. Finally, no significant changes were detected in the spectra recorded on pure CeO_2, which in fact resulted to be the least active material. These results confirm the key role of the catalyst reducibility in case of the CO oxidation reaction; this property can be evaluated through the extent of the intensity increase and of the formation rate of the D3 band at high temperature, but is interestingly related to a rise of the non-reduced defect sites at RT. Thanks to the quick rearrangement of the structure in Ce95Cu5, evidenced by marked spectral changes, this catalyst is the most suitable one to further deepen the understanding of this phenomenon. Therefore, time-resolved Raman analyses were carried out on the Ce95Cu5 sample during the first 10 minutes of reaction, studying the effect of CO concentration on the structural disorder.

Two cycles of reduction and oxidation were repeated, using 1000 and 2000 ppm of CO in N_2 as reducing mixture. For what concerns the Raman spectra collected at 400 °C after 40 minutes from each gas change, the results appear similar at the two CO concentrations (see Fig. 8B at 1000 ppm and Fig. S13 at 2000 ppm). Nevertheless, some differences could be noticed when the evolution of the spectra was monitored during the gas change from pure N_2 to the CO/N_2 mixture, through the continuous acquisition of Raman spectra during the first 10 minutes of reaction. As it can be appreciated from the time series collected at 1000 and 2000 ppm of CO (Fig. 10 A and B, respectively) the increase of the contribution of the D3 component occurred in the first minutes of exposure to CO and was associated with a marked intensity drop and with a broadening of the F_{2g} peak. For this reason, a comparison based on the calculation of the D/F_{2g} ratio may not be reliable: in fact, as previously discussed, the changes in the F_{2g} peak induced by the appearance of new defects could lead to misinterpretation in the microstructural analysis.
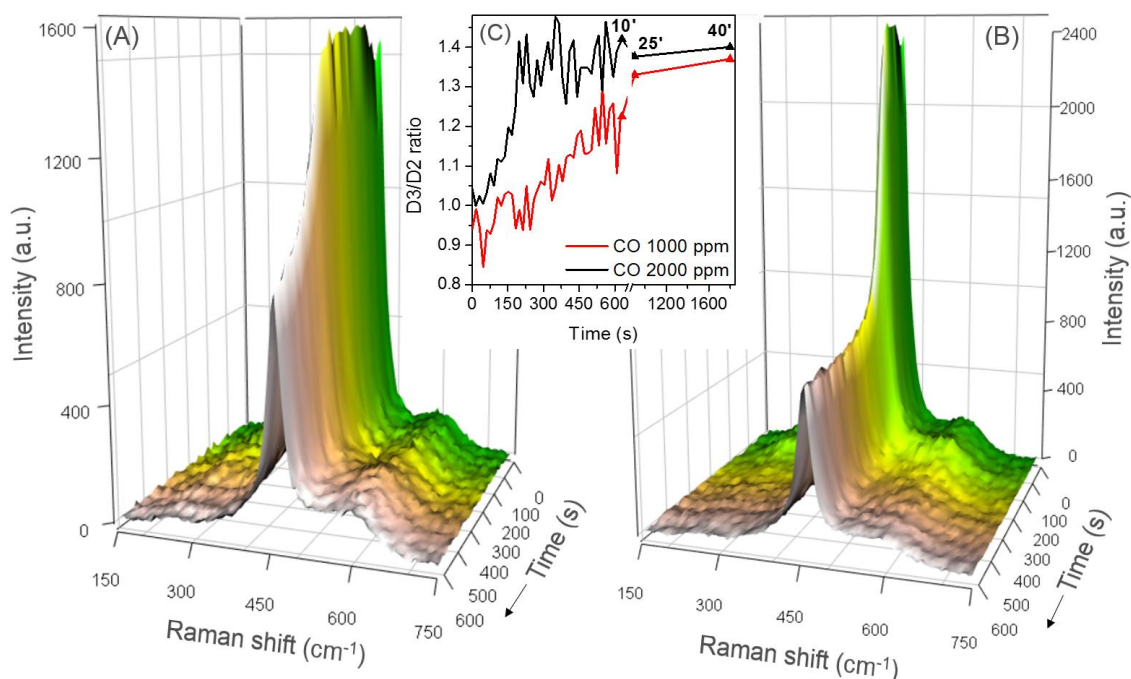

Fig. 10. Time evolution of the Raman spectra collected on the Ce95Cu5 catalyst at 400°C after switching the gas flow from pure N_2 to a mixture of 1000 (A) or 2000 (B) ppm of CO in N_2. In the inset (C) the trend of the D3/D2 intensity ratio is reported.

However, since the D3 defects form in reducing conditions, while the D2 peak is related to oxidized sites, the D3/D2 ratio could provide an indication of the reduction state of the sample. The evolution of the spectrum after sending CO in the cell can be thereby followed by tracking this parameter, whose trend is compared at 1000 and 2000 ppm of CO in the inset of Fig. 10. The calculated curves show an almost linear increase of the D3/D2 ratio after flowing the gas, which reaches a stable value after around 200 s only at the higher CO concentration. An incipient plateau is reached also at 1000 ppm, but at later times, after more than 25 minutes. In the presence of a higher CO concentration the changes occurred earlier, confirming an increased reaction rate; on the other hand, the mean values of the D3/D2 ratio at saturation only showed minor changes, rising from 1.37 to 1.4. This result points out the dependence of the spectrum on the CO concentration: a higher quantity of CO in the gas only slightly affects the amount of vacancies generated at the equilibrium, but it enhances their formation rate. However, the development of oxygen vacancies associated to reduced cations seems to be a consequence of the catalytic conversion of CO, rather than the activation mechanism. This outcome is also consistent with the absence of a strong D3 component during the conversion of CO in air, which suggests that the oxidation step of the catalytic cycle (vacancy refilling) is faster than the reduction one (vacancy formation) in line with the findings of Kopelent et al. [63]. Actually, the absence of O_2 in the atmosphere allows to capture the release of lattice oxygen, which seems to form stable vacancies only in oxygen poor conditions.

In order to verify if the D3 defects generated at 400 °C could be stable at RT, a final test was carried out on the Ce95Cu5 sample: the catalyst was heated up to 400 °C, then a cycle of reduction in 1000 ppm of CO in N_2 followed by oxidation in O_2 was performed; afterwards, the CO/N_2 mixture was sent into the cell and after 40 min the sample was cooled to RT in this atmosphere; finally, the catalyst was exposed to O_2. The spectra collected at RT before and after this test are reported in Fig. 11, together with a scheme of the test schedule.
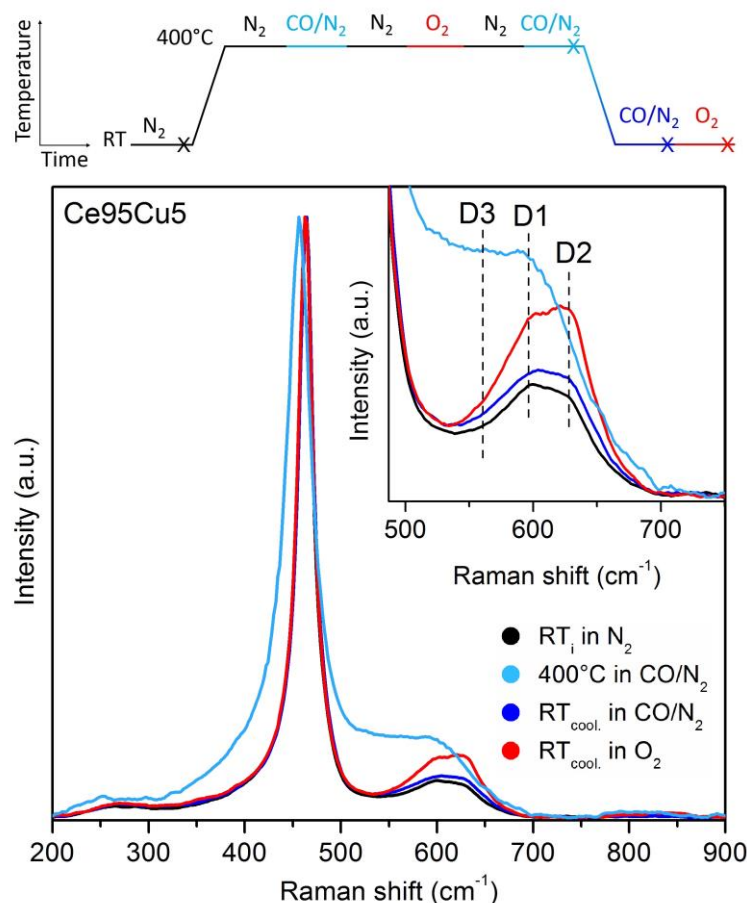

Fig. 11. Raman spectra acquired during the in-situ analyses performed on the Ce95Cu5 sample during cycles of reduction and oxidation: at the beginning of the test (RT_i), at 400°C after 40 minutes in CO 1000 ppm/N_2, at the end of the test ($RT_{cool.}$) at RT in CO 1000 ppm/N_2 and after the exposure to oxygen. In the inset, a magnification of the defect band is shown. The spectra were normalized to the intensity of the F_{2g} peak. The scheme above the picture briefly resumes how the test was performed, and the crosses indicate when the spectra shown in the figure were collected.

The intense D3 band observed at 400 °C almost completely disappeared during the cooling phase, before exposing the sample to oxygen. However, the D band, which preserved its original shape, was more intense after the test (+15%) suggesting that a moderate quantity of new D1 and D2 defects was generated during the cycle. Finally, in oxidizing conditions, a remarkable increase of the D band was observed (+81%): this confirms that the D1 and D2 defects predominantly form in presence of oxygen; moreover, these changes were emphasized when the structure of the material had been previously affected by the exposure to CO.

These last results raise questions about the precursors of the additional D1 and D2 sites, which cannot be only created through a direct oxygen vacancy refilling mechanism. Indeed, neither the disappearance of the D3 band nor the rise of the D2 band are associated to a corresponding increase or decrease of another defect component, as could be expected. A possible explanation could derive from the clustering of oxygen vacancies under reducing conditions, which could be associated to the formation of reduced sites consisting both in Cu clusters at the catalyst surface and Ce^{3+} cations. In this case, a scheme illustrating the behaviour of the oxygen vacancies during the tests is depicted in Fig. 12. Multiple vacancy clusters, whose existence has been hypothesized and proved by different authors [33,36,64–66], could provide the broad and unresolved D3 band and better explain the huge decrease of the intensity of the F_{2g} mode as a consequence of a greater disruption of the structural order [66]. Moreover, the presence of small copper clusters was previously proposed by Elias et al. [67] according to their in situ XANES (X-ray absorption near-edge spectroscopy) and EXAFS (extended X-ray absorption fine structure) measurements performed on 10% Cu doped ceria catalysts in CO atmosphere. Such metallic copper sites exhibited a reversible behaviour upon reoxidation, as also detected in a different study by in-situ XRD analyses that evidenced the cyclic appearance of metallic Cu reflections during H_2/O_2 alternating exposure of Cu-containing ceria.[68] A similar reversible clustering mechanism was described also for Pd-containing perovskite [69]. However, in the present study, the reversibility is already detected by lowering the temperature and therefore by decreasing the conversion rate of CO. Such behaviour can be consistent with the reorganization of surface vacancy clusters due to the diffusion of bulk oxygen to the surface when the rate of CO oxidation is decreased and the reaction finally stops. Nevertheless, isolated oxygen vacancies can still be present and can readily be refilled by molecular oxygen dissociation upon reoxidation of the sample. This process can reasonably lead to the formation of new D2 and D1 defects and can explain why the catalysts which did not undergo analogous structural modifications during CO oxidation showed a smaller or negligible increase of these components at the end of the reaction. The reason behind such dissimilar behaviour during and after CO conversion may eventually be found in the different redox properties of the dopants (Cu ions features the highest reducibility in the set) and their consequent different tendency to form aggregated reduced sites in conjunction with the formation of oxygen vacancies in the ceria lattice.
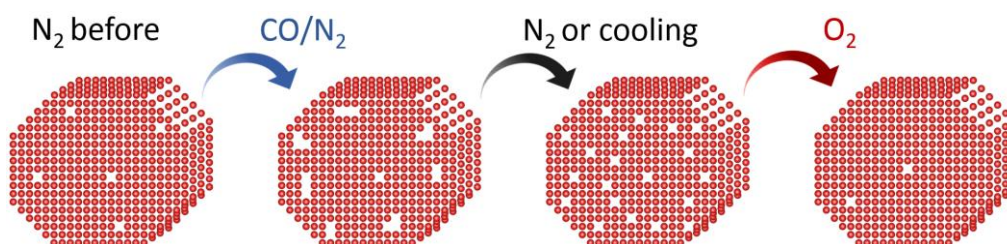

Fig. 12. Simplified scheme illustrating the evolution of the oxygen vacancies during the different tests performed on the Ce95Cu5 catalyst; the red spheres represent the oxygen ions in the ceria lattice, while the cations are not shown for the sake of clarity.

4. Conclusions

In the present work, the CO oxidation reaction was studied by in situ Raman spectroscopy on four different nanostructured ceria-based materials (CeO$_2$, Ce95Cu5, Ce95Mn5 and Ce95Cu2.5Mn2.5) in order to investigate the relationship between their catalytic activity and defectiveness.

A higher defect density, evaluated through the calculation of the D/F$_{2g}$ Raman band ratio, and new extrinsic defect sites were detected in the doped samples at RT, consistently with the good dispersion of the dopant cations in ceria matrix

suggested by TEM. In situ Raman analyses during the CO oxidation allowed then to monitor structural evolution in operando conditions. While the changes in the defect band were limited and possibly masked by temperature effects, the spectra acquired during these tests evidenced the formation of polyene-like chains on the surface of the CeO_2 and Ce95Cu5 catalysts before their activation towards CO oxidation. Such results may be an evidence of the existence of CO disproportionation (i.e. of a dissociative adsorption) also in oxidizing conditions at low temperature.

Comparing the Raman spectra recorded at RT before and after CO oxidation, reversibility was observed only for pure CeO_2. Instead, the doped samples exhibited a rise of the D band, which was especially marked for the two Cu-doped materials.

The interaction between the catalysts and CO at the origin of these changes was further investigated by in situ Raman analyses during cycles of reduction (CO in N_2) and oxidation (pure O_2) at 400 °C. Pure ceria confirmed its higher stability, while the Ce95Cu5 sample exhibited remarkable variations: a broad band around 550 cm^{-1} (D3) appeared in reducing conditions, pointing out the formation of oxygen vacancies in the lattice, that were quickly refilled when flowing O_2, together with an increase of the high Raman shift defect bands (D1 and D2).

While D3 defects could be observed in the high temperature Raman spectra, it was not possible to preserve them at RT, even without switching to oxidant atmospheres; these last results suggest that the very broad features of the D3 defects are more likely related to vacancy clusters. When CO oxidation ceases as a consequence of the temperature decrease, these clusters are readily reorganized in isolated vacancies, which can be the precursors of the oxidized D1 and D2 defect sites appearing in oxygen.

The two Mn-doped samples were characterized by a less marked growth of the D3 band during the exposure to CO. Interestingly, a correlation between the D3 intensity and formation rate in reducing conditions and the catalytic activity was found, suggesting that the D3 sites are formed as a consequence of the catalytic oxidation, as also supported by the observed dependence on the CO concentration. Moreover, the greater reducibility was associated to a stronger increase of the Frenkel sites and oxidized defects components (D1 and D2) once returned to RT, consistently with the involvement of the defect sites in a more pronounced structural rearrangement, fostered by the presence of easily reducible dopants.

Although further investigations are required in order to extend the results to other types of ceria-based materials, the tests carried out in different atmospheres allowed to unveil some interesting mechanisms which contribute in defining the catalyst reducibility and reactivity, leading to outcomes which are worth considering in the framework of designing active catalysts.

Declaration of interest

The authors declare no competing interests.

Appendix A. Supplementary data

Supplementary material related to this article can be found, in the online version, at doi:

References

[1]   Z. Zhang, Z. Jiang, W. Shangguan, Low-temperature catalysis for VOCs removal in technology and application: A state-of-the-art review, Catal. Today. 264 (2016) 270–278. doi:10.1016/j.cattod.2015.10.040.
[2]   H. Osgood, S. V. Devaguptapu, H. Xu, J. Cho, G. Wu, Transition metal (Fe, Co, Ni, and Mn) oxides for oxygen reduction and evolution bifunctional catalysts in alkaline media, Nano Today. 11 (2016) 601–625. doi:10.1016/J.NANTOD.2016.09.001.
[3]   T. Montini, M. Melchionna, M. Monai, P. Fornasiero, Fundamentals and Catalytic Applications of CeO2-Based Materials, Chem. Rev. 116 (2016) 5987–6041. doi:10.1021/acs.chemrev.5b00603.
[4]   A. Trovarelli, P. Fornasiero, Catalysis by Ceria and Related Materials, IMPERIAL COLLEGE PRESS, 2013. doi:10.1142/p870.
[5]   M. Piumetti, T. Andana, S. Bensaid, N. Russo, D. Fino, R. Pirone, Study on the CO Oxidation over Ceria-Based Nanocatalysts, Nanoscale Res. Lett. 11 (2016) 165. doi:10.1186/s11671-016-1375-z.
[6]   D. Mukherjee, B.G. Rao, B.M. Reddy, CO and soot oxidation activity of doped ceria: Influence of dopants, Appl. Catal. B Environ. 197 (2016) 105–115. doi:10.1016/j.apcatb.2016.03.042.

[7] R. Fiorenza, C. Crisafulli, G.G. Condorelli, F. Lupo, S. Scirè, Au–Ag/CeO2 and Au–Cu/CeO2 Catalysts for Volatile Organic Compounds Oxidation and CO Preferential Oxidation, Catal. Letters. 145 (2015) 1691–1702. doi:10.1007/s10562-015-1585-5.

[8] A. Bueno-López, Diesel soot combustion ceria catalysts, Appl. Catal. B Environ. 146 (2014) 1–11. doi:10.1016/j.apcatb.2013.02.033.

[9] S. Liu, X. Wu, D. Weng, R. Ran, Ceria-based catalysts for soot oxidation: A review, J. Rare Earths. 33 (2015) 567–590. doi:10.1016/S1002-0721(14)60457-9.

[10] C. Ratnasamy, J.P. Wagner, Water Gas Shift Catalysis, Catal. Rev. 51 (2009) 325–440. doi:10.1080/01614940903048661.

[11] D.R. Mullins, The surface chemistry of cerium oxide, Surf. Sci. Rep. 70 (2015) 42–85. doi:10.1016/j.surfrep.2014.12.001.

[12] M. Piumetti, S. Bensaid, T. Andana, M. Dosa, C. Novara, F. Giorgis, N. Russo, D. Fino, Nanostructured Ceria-Based Materials: Effect of the Hydrothermal Synthesis Conditions on the Structural Properties and Catalytic Activity, Catalysts. 7 (2017) 174. doi:10.3390/catal7060174.

[13] A. Trovarelli, J. Llorca, Ceria Catalysts at Nanoscale: How Do Crystal Shapes Shape Catalysis?, ACS Catal. 7 (2017) 4716–4735. doi:10.1021/acscatal.7b01246.

[14] M. Guo, W. Yin, F. Zhao, Q. Wang, C. Hu, Nanostructured Ceria-Praseodymium and Ceria-Terbium Mixed Oxides: Relationship Between Structural Change and Catalytic Activity Towards CO Oxidation, J. Nanosci. Nanotechnol. 19 (2019) 5999–6005. doi:10.1166/jnn.2019.16542.

[15] Y. Wang, H.J. Su, S.D. Wang, Ceria nanocube with reactive {100} exposure planes: Simple and controllable synthesis under moderate conditions, Ceram. Int. 45 (2019) 15199–15204. doi:10.1016/j.ceramint.2019.05.004.

[16] G. Spezzati, A.D. Benavidez, A.T. DeLaRiva, Y. Su, J.P. Hofmann, S. Asahina, E.J. Olivier, J.H. Neethling, J.T. Miller, A.K. Datye, E.J.M. Hensen, CO oxidation by Pd supported on CeO 2 (100) and CeO 2 (111) facets, Appl. Catal. B Environ. 243 (2019) 36–46. doi:10.1016/j.apcatb.2018.10.015.

[17] Z. Wu, M. Li, S.H. Overbury, On the structure dependence of CO oxidation over CeO2nanocrystals with well-defined surface planes, J. Catal. 285 (2012) 61–73. doi:10.1016/j.jcat.2011.09.011.

[18] A. Filtschew, K. Hofmann, C. Hess, Ceria and Its Defect Structure: New Insights from a Combined Spectroscopic Approach, J. Phys. Chem. C. 120 (2016) 6694–6703. doi:10.1021/acs.jpcc.6b00959.

[19] S. Royer, D. Duprez, Catalytic Oxidation of Carbon Monoxide over Transition Metal Oxides, ChemCatChem. 3 (2011) 24–65. doi:10.1002/cctc.201000378.

[20] R.J. Baxter, P. Hu, Insight into why the Langmuir-Hinshelwood mechanism is generally preferred, J. Chem. Phys. 116 (2002) 4379–4381. doi:10.1063/1.1458938.

[21] E.K. Dann, E.K. Gibson, C.R.A. Catlow, V. Celorrio, P. Collier, T. Eralp, M. Amboage, C. Hardacre, C. Stere, A. Kroner, A. Raj, S. Rogers, A. Goguet, P.P. Wells, Combined spatially resolved operando spectroscopy: New insights into kinetic oscillations of CO oxidation on Pd/Γ-Al2O3, J. Catal. 373 (2019) 201–208. doi:10.1016/j.jcat.2019.03.037.

[22] B. Liu, W. Li, W. Song, J. Liu, Carbonate-mediated Mars-van Krevelen mechanism for CO oxidation on cobalt-doped ceria catalysts: Facet-dependence and coordination-dependence, Phys. Chem. Chem. Phys. 20 (2018) 16045–16059. doi:10.1039/c8cp01694a.

[23] Y. Sun, C. Li, I. Djerdj, O. Khalid, P. Cop, J. Sann, T. Weber, S. Werner, K. Turke, Y. Guo, B.M. Smarsly, H. Over, Oxygen storage capacity versus catalytic activity of ceria-zirconia solid solutions in CO and HCl oxidation, Catal. Sci. Technol. 9 (2019) 2163–2172. doi:10.1039/c9cy00222g.

[24] M. Piumetti, S. Bensaid, N. Russo, D. Fino, Investigations into nanostructured ceria-zirconia catalysts for soot combustion, Appl. Catal. B Environ. 180 (2016) 271–282. doi:10.1016/j.apcatb.2015.06.018.

[25] A. Trovarelli, Structural and Oxygen Storage/Release Properties of CeO2 -Based Solid Solutions, Comments Inorg. Chem. 20 (1999) 263–284. doi:10.1080/02603599908021446.

[26] T. Andana, M. Piumetti, S. Bensaid, L. Veyre, C. Thieuleux, N. Russo, D. Fino, E.A. Quadrelli, R. Pirone, Nanostructured equimolar ceria-praseodymia for NOx-assisted soot oxidation: Insight into Pr dominance over Pt nanoparticles and metal–support interaction, Appl. Catal. B Environ. 226 (2018) 147–161. doi:10.1016/j.apcatb.2017.12.048.

[27] M. Piumetti, S. Bensaid, T. Andana, N. Russo, R. Pirone, D. Fino, Cerium-copper oxides prepared by solution combustion synthesis for total oxidation reactions: From powder catalysts to structured reactors, Appl. Catal. B Environ. 205 (2017) 455–468. doi:10.1016/j.apcatb.2016.12.054.

[28] Y. Gao, X. Wu, S. Liu, D. Weng, R. Ran, MnOx–CeO2 mixed oxides for diesel soot oxidation: a review, Catal. Surv. from Asia. 22 (2018) 230–240. doi:10.1007/s10563-018-9255-4.

[29] K. Kappis, C. Papadopoulos, J. Papavasiliou, J. Vakros, Y. Georgiou, Y. Deligiannakis, G. Avgouropoulos, Tuning the catalytic properties of copper-promoted nanoceria via a hydrothermal method, Catalysts. 9 (2019). doi:10.3390/catal9020138.

[30] P. Venkataswamy, D. Jampaiah, D. Mukherjee, C.U. Aniz, B.M. Reddy, Mn-doped Ceria Solid Solutions for CO Oxidation at Lower Temperatures, Catal. Letters. 146 (2016) 2105–2118. doi:10.1007/s10562-016-1811-9.

[31] F. Zhao, S. Li, X. Wu, R. Yue, W. Li, Y. Chen, Synergetic effect over flame-made manganese doped CuO-CeO

2 nanocatalyst for enhanced CO oxidation performance, RSC Adv. 9 (2019) 2343–2352. doi:10.1039/c8ra09626k.

[32]   Y. Zhao, B.T. Teng, X.D. Wen, Y. Zhao, Q.P. Chen, L.H. Zhao, M.F. Luo, Superoxide and peroxide species on CeO 2(111), and their oxidation roles, J. Phys. Chem. C. 116 (2012) 15986–15991. doi:10.1021/jp3016326.

[33]   L. Wang, Y. Yu, H. He, Y. Zhang, X. Qin, B. Wang, Oxygen vacancy clusters essential for the catalytic activity of CeO2 nanocubes for o-xylene oxidation, Sci. Rep. 7 (2017) 1–11. doi:10.1038/s41598-017-13178-6.

[34]   C. Papadopoulos, K. Kappis, J. Papavasiliou, J. Vakros, M. Kuśmierz, W. Gac, Y. Georgiou, Y. Deligiannakis, G. Avgouropoulos, Copper-promoted ceria catalysts for CO oxidation reaction, Catal. Today. (2019) 1–7. doi:10.1016/j.cattod.2019.06.078.

[35]   J.A. Sullivan, P. Dulgheru, I. Atribak, A. Bueno-López, A. García-García, Attempts at an in situ Raman study of ceria/zirconia catalysts in PM combustion, Appl. Catal. B Environ. 108–109 (2011) 134–139. doi:10.1016/j.apcatb.2011.08.018.

[36]   S. Agarwal, X. Zhu, E.J.M. Hensen, L. Lefferts, B.L. Mojet, Defect chemistry of ceria nanorods, J. Phys. Chem. C. 118 (2014) 4131–4142. doi:10.1021/jp409989y.

[37]   E. Sartoretti, C. Novara, F. Giorgis, M. Piumetti, S. Bensaid, N. Russo, D. Fino, In situ Raman analyses of the soot oxidation reaction over nanostructured ceria-based catalysts, Sci. Rep. 9 (2019) 3875. doi:10.1038/s41598-019-39105-5.

[38]   C. Schilling, C. Hess, Real-Time Observation of the Defect Dynamics in Working Au/CeO2 Catalysts by Combined Operando Raman/UV-Vis Spectroscopy, J. Phys. Chem. C. 122 (2018) 2909–2917. doi:10.1021/acs.jpcc.8b00027.

[39]   M. Dosa, M. Piumetti, S. Bensaid, T. Andana, C. Novara, F. Giorgis, D. Fino, N. Russo, Novel Mn–Cu-Containing CeO2 Nanopolyhedra for the Oxidation of CO and Diesel Soot: Effect of Dopants on the Nanostructure and Catalytic Activity, Catal. Letters. 148 (2018) 298–311. doi:10.1007/s10562-017-2226-y.

[40]   M. Lykaki, E. Pachatouridou, S.A.C. Carabineiro, E. Iliopoulou, C. Andriopoulou, N. Kallithrakas-Kontos, S. Boghosian, M. Konsolakis, Ceria nanoparticles shape effects on the structural defects and surface chemistry: Implications in CO oxidation by Cu/CeO2catalysts, Appl. Catal. B Environ. 230 (2018) 18–28. doi:10.1016/j.apcatb.2018.02.035.

[41]   H.X. Mai, L.D. Sun, Y.W. Zhang, R. Si, W. Feng, H.P. Zhang, H.C. Liu, C.H. Yan, Shape-selective synthesis and oxygen storage behavior of ceria nanopolyhedra, nanorods, and nanocubes, J. Phys. Chem. B. 109 (2005) 24380–24385. doi:10.1021/jp055584b.

[42]   C. Artini, M. Pani, M.M. Carnasciali, M.T. Buscaglia, J.R. Plaisier, G.A. Costa, Structural features of Sm- and Gd-doped ceria studied by synchrotron X-ray diffraction and -raman spectroscopy, Inorg. Chem. 54 (2015) 4126–4137. doi:10.1021/acs.inorgchem.5b00395.

[43]   M. Lohrenscheit, C. Hess, Direct Evidence for the Participation of Oxygen Vacancies in the Oxidation of Carbon Monoxide over Ceria-Supported Gold Catalysts by using Operando Raman Spectroscopy, ChemCatChem. 8 (2016) 523–526. doi:10.1002/cctc.201501129.

[44]   I.D.C. Silva, F.A. Sigoli, I.O. Mazali, Reversible Oxygen Vacancy Generation on Pure CeO2 Nanorods Evaluated by in Situ Raman Spectroscopy, J. Phys. Chem. C. 121 (2017) 12928–12935. doi:10.1021/acs.jpcc.7b03155.

[45]   Y. Lee, G. He, A.J. Akey, R. Si, M. Flytzani-Stephanopoulos, I.P. Herman, Raman analysis of mode softening in nanoparticle CeO2-δ and Au-CeO2-δ during CO oxidation, J. Am. Chem. Soc. 133 (2011) 12952–12955. doi:10.1021/ja204479j.

[46]   Z. Wu, M. Li, J. Howe, H.M. Meyer, S.H. Overbury, Probing defect sites on CeO2 nanocrystals with well-defined surface planes by raman spectroscopy and O2 adsorption, Langmuir. 26 (2010) 16595–16606. doi:10.1021/la101723w.

[47]   S. Agarwal, X. Zhu, E.J.M. Hensen, B.L. Mojet, L. Lefferts, Surface-Dependence of Defect Chemistry of Nanostructured Ceria, J. Phys. Chem. C. 119 (2015) 12423–12433. doi:10.1021/acs.jpcc.5b02389.

[48]   C. Andriopoulou, A. Trimpalis, K.C. Petallidou, A. Sgoura, A.M. Efstathiou, S. Boghosian, Structural and Redox Properties of Ce 1− x Zr x O 2−δ and Ce 0.8 Zr 0.15 RE 0.05 O 2−δ (RE: La, Nd, Pr, Y) Solids Studied by High Temperature in Situ Raman Spectroscopy, J. Phys. Chem. C. 121 (2017) 7931–7943. doi:10.1021/acs.jpcc.7b00515.

[49]   L. Li, F. Chen, J.-Q. Lu, M.-F. Luo, Study of defect sites in Ce1-xMxO2-δ (x = 0.2) solid solutions using Raman spectroscopy., J. Phys. Chem. A. 115 (2011) 7972–7. doi:10.1021/jp203921m.

[50]   K. Polychronopoulou, A.F. Zedan, M. AlKetbi, S. Stephen, M. Ather, M.S. Katsiotis, J. Arvanitidis, D. Christofilos, A.F. Isakovic, S. AlHassan, Tailoring the efficiency of an active catalyst for CO abatement through oxidation reaction: The case study of samarium-doped ceria, J. Environ. Chem. Eng. 6 (2018) 266–280. doi:10.1016/j.jece.2017.12.001.

[51]   T. Vinodkumar, B.G. Rao, B.M. Reddy, Influence of isovalent and aliovalent dopants on the reactivity of cerium oxide for catalytic applications, Catal. Today. 253 (2015) 57–64. doi:10.1016/j.cattod.2015.01.044.

[52]   S.A. Acharya, V.M. Gaikwad, S.W. D'Souza, S.R. Barman, Gd/Sm dopant-modified oxidation state and defect generation in nano-ceria, Solid State Ionics. 260 (2014) 21–29. doi:10.1016/j.ssi.2014.03.008.

[53]   T. Taniguchi, T. Watanabe, N. Sugiyama, A.K. Subramani, H. Wagata, N. Matsushita, M. Yoshimura, Identifying defects in ceria-based nanocrystals by UV resonance Raman spectroscopy, J. Phys. Chem. C. 113 (2009) 19789–19793. doi:10.1021/jp9049457.

[54]   A.N. Da Silva, R.C.F. Pinto, P.T.C. Freire, J.A.L. Junior, A.C. Oliveira, J.M. Filho, Temperature and high pressure effects on the structural features of catalytic nanocomposites oxides by Raman spectroscopy, Spectrochim. Acta - Part A Mol. Biomol. Spectrosc. 138 (2015) 763–773. doi:10.1016/j.saa.2014.11.081.

[55]   H. Zhu, Y. Chen, Z. Wang, W. Liu, L. Wang, Catalytic oxidation of CO over mesoporous copper-doped ceria catalysts via a facile CTAB-assisted synthesis, RCS Adv. (2018) 14888–14897. doi:10.1039/c8ra02327a.

[56]   P. Bera, A. Lo, A. Horne, A. Martı, Comparative in Situ DRIFTS-MS Study of 12 CO- and 13 CO-TPR on CuO / CeO 2 Catalyst, (2009) 10689–10695.

[57]   H.E. Schaffer, R.R. Chance, R.J. Silbey, K. Knoll, R.R. Schrock, Conjugation length dependence of Raman scattering in a series of linear polyenes: Implications for polyacetylene, J. Chem. Phys. 94 (1991) 4161–4170. doi:10.1063/1.460649.

[58]   R.F. Fernandes, L.F. Maia, M.R.C. Couri, L.A.S. Costa, L.F.C. De Oliveira, Raman spectroscopy as a tool in differentiating conjugated polyenes from synthetic and natural sources, Spectrochim. Acta - Part A Mol. Biomol. Spectrosc. 134 (2015) 434–441. doi:10.1016/j.saa.2014.06.022.

[59]   M. Swanson, V. V. Pushkarev, V.I. Kovalchuk, J.L. D 'itri, J.L. D'itri, The dynamic surface chemistry during the interaction of CO with ceria captured by Raman spectroscopy, Catal. Letters. 116 (2007) 41–45. doi:10.1007/s10562-007-9087-8.

[60]   B. Böller, K.M. Durner, J. Wintterlin, The active sites of a working Fischer−Tropsch catalyst revealed by operando scanning tunnelling microscopy, Nat. Catal. (2019). doi:10.1038/s41929-019-0360-1.

[61]   J.E. Spanier, R.D. Robinson, F. Zhang, S.-W. Chan, I.P. Herman, Size-dependent properties of CeO2-y nanoparticles as studied by Raman scattering, Phys. Rev. B. 64 (2001) 245407. doi:10.1103/PhysRevB.64.245407.

[62]   J.R. McBride, K.C. Hass, B.D. Poindexter, W.H. Weber, Raman and x-ray studies of Ce1-xRExO2-y, where RE=La, Pr, Nd, Eu, Gd, and Tb, J. Appl. Phys. 76 (1994) 2435–2441. doi:10.1063/1.357593.

[63]   R. Kopelent, J.A. Van Bokhoven, J. Szlachetko, J. Edebeli, C. Paun, M. Nachtegaal, O. V. Safonova, Catalytically Active and Spectator Ce3+ in Ceria-Supported Metal Catalysts, Angew. Chemie - Int. Ed. 54 (2015) 8728–8731. doi:10.1002/anie.201503022.

[64]   L. Xiangwen, Z. Kebin, W. Lei, W. Baoyi, L. Yadong, Oxygen vacancy clusters promoting reducibility and activity of ceria nanorods, J. Am. Chem. Soc. 131 (2009) 3140–3141. http://www.scopus.com/scopus/inward/record.url?eid=2-s2.0-63849333291&partnerID=40.

[65]   H. Wang, S. Luo, M. Zhang, W. Liu, X. Wu, S. Liu, Roles of oxygen vacancy and Ox− in oxidation reactions over CeO2 and Ag/CeO2 nanorod model catalysts, J. Catal. 368 (2018) 365–378. doi:10.1016/j.jcat.2018.10.018.

[66]   S. Pal, N. Gogurla, A. Das, S.S. Singha, P. Kumar, D. Kanjilal, A. Singha, S. Chattopadhyay, D. Jana, A. Sarkar, Clustered vacancies in ZnO: Chemical aspects and consequences on physical properties, J. Phys. D. Appl. Phys. 51 (2018). doi:10.1088/1361-6463/aaa992.

[67]   J.S. Elias, K.A. Stoerzinger, W.T. Hong, M. Risch, L. Giordano, A.N. Mansour, Y. Shao-Horn, In situ spectroscopy and mechanistic insights into CO oxidation on transition-metal-substituted ceria nanoparticles, ACS Catal. 7 (2017) 6843–6857. doi:10.1021/acscatal.7b01600.

[68]   K. Kappis, J. Papavasiliou, Influence of the Hydrothermal Parameters on the Physicochemical Characteristics of Cu−Ce Oxide Nanostructures, ChemCatChem. 11 (2019) 4765–4776. doi:10.1002/cctc.201901108.

[69]   J. Li, U.G. Singh, J.W. Bennett, K. Page, J.C. Weaver, J. Zhang, T. Proffen, A.M. Rappe, S. Scott, R. Seshadri, BaCe 1-x Pd x O 3-δ (0 e x e 0 . 1): Redox Controlled Ingress and Egress of Palladium in a Perovskite, Chem. Mater. 19 (2007) 1418–1426.